

ARTICLE

OPEN



Direct growth of orthorhombic $\text{Hf}_{0.5}\text{Zr}_{0.5}\text{O}_2$ thin films for hysteresis-free MoS_2 negative capacitance field-effect transistors

Hae Won Cho^{1,4}, Pavan Pujar^{1,4}, Minsu Choi², Seunghun Kang³, Seongin Hong¹, Junwoo Park¹, Seungho Baek¹, Yunseok Kim³✉, Jaichan Lee¹✉ and Sunkook Kim¹✉

Herein, the direct growth of polar orthorhombic phase in $\text{Hf}_{0.5}\text{Zr}_{0.5}\text{O}_2$ (HZO) thin films is reported using Pulsed Laser Deposition (PLD). The growth of HZO onto a preheated (700 °C) silicon substrate mimics the rapid thermal annealing, which allows the formation of smaller crystallites (~9.7 nm) with large surface energy leading to the stabilization of metastable orthorhombic phase. Unlike atomic layer deposition (ALD) of HZO, PLD is more advantageous for depositing highly crystalline thin films through optimized parameters, such as laser fluence and background gas pressure. Further, the PLD-HZO is integrated with HfO_2 dielectric and the resulting gate stacks have been used in the bottom gate FET architecture-'Si//PLD-HZO/ HfO_2 / MoS_2 /Ti/Au'. The NCFETs have yielded a sub-thermionic subthreshold swing ($SS_{for} = 33.03 \pm 8.7 \text{ mV/dec.}$ and $SS_{rev} = 36.4 \pm 7.7 \text{ mV/dec.}$) and a negligible hysteresis (~28 mV), which is capable in realizing low power integrated digital/analog circuits.

npj 2D Materials and Applications (2021)5:46; <https://doi.org/10.1038/s41699-021-00229-w>

INTRODUCTION

Incorporation of a thin ferroelectric layer in the gate stack of Field Effect Transistors (FETs) is an innovative approach to achieve steep switching and hysteresis-free devices^{1,2}. Among the widely available options of ferroelectric materials, ranging from metal oxides to polymers, metal oxides have gained considerable technological importance owing to their compatibility with current complementary-metal-oxide-semiconductor (CMOS) technology as well as large-scale integration³. A well-known, high dielectric permittivity (κ) hafnium oxide (HfO_2) can also act as a ferroelectric with proper modification in the crystal structure. In other words, amorphous HfO_2 is the most popular high κ dielectric; but, its crystalline counterpart with metastable-orthorhombic phase (o-phase, $Pca2_1$) depicts large remnant polarization due to inherent ferroelectricity originated from the displacement of oxygen anions (i.e., non-centrosymmetry). The stabilization of o-phase is challenging due to the affinity of HfO_2 toward the thermodynamically stable, monoclinic phase (m-phase, $P2_1/c$)³. However, numerous ways have been established to crystallize the as-deposited thin films of HfO_2 into prominent o-phase, such as - substitutional doping (Zr, Al, La, and so on)⁴⁻⁶, achieving finer grains with large surface energy⁷, encapsulating with electrodes⁸, depositing via distinct techniques such as Atomic Layer Deposition (ALD), Chemical Solution Deposition (CSD) and designing specific processing conditions such as annealing temperature, time, and heating/cooling rates⁹. Notably, high heating rates are often required to restrict grain growth, which leads to the formation of finer grains with a large grain boundary area. Besides, low-temperature (<250 °C) growth using ALD is the most popular and widely reported deposition method, which demands an additional crystallization process. The low-temperature deposition through precursors retains the

carbonaceous impurities at the junctions of as-deposited granular domains¹⁰, which significantly hampers the growth when subjected to post-processing, such as rapid thermal annealing. Given this analogy, the post-processing-crystallization step is unavoidable as far as ALD and/or CSD techniques are concerned. Thus, an additional processing step is always necessary to achieve outstanding ferroelectric properties. In this regard, the present work demonstrates the possibility of direct growth of o-phase in Zr doped HfO_2 ($\text{Hf}_{0.5}\text{Zr}_{0.5}\text{O}_2$: HZO) on Si substrate, with finer crystallites using PLD technique. Of course, a lot of research on the growth of HZO on various substrates with the PLD process has been conducted, confirming the case with excellent ferroelectric phase¹¹⁻¹³. In this study, prominent o-phase was obtained by growing directly on the Si substrate for ferroelectric response. Substrate selection was also intended to show that it can be used as a useful device in an industry that is currently focused on silicon processing, and a two-dimensional (2D) molybdenum disulfide (MoS_2) NCFETs was investigated based on the grown HZO thin films. Despite tunable bandgap and colossal theoretical high carrier mobility (at room temperature) MoS_2 based FETs suffer from various instabilities, such as large hysteresis, threshold voltage, and high subthreshold swing (SS). The origin of instabilities is attributed to the prodigious surface area of MoS_2 , which allows the atmospheric gas molecules to chemically adsorb on to the surface, resulting in hindered transport of charge carriers. These instabilities are generally observed regardless of the device architecture and channel layer thickness. Furthermore, high SS magnitudes demand increased power inputs, thereby promoting the heating effect. Thus, the problem of power dissipation becomes more severe in the case of large-scale integration of billions of FETs. The fundamental thermionic limit restricts the magnitude of SS to 60 mV/dec at room temperature^{14,15}. Among

¹Multifunctional Nano Bio Electronics Lab, School of Advanced Materials Science and Engineering, Sungkyunkwan University, Gyeonggi-do, Suwon, South Korea. ²Emergent Materials Design Lab, School of Advanced Materials Science and Engineering, Sungkyunkwan University, Gyeonggi-do, Suwon, South Korea. ³Multiscale Materials Imaging Lab, School of Advanced Materials Science and Engineering, Sungkyunkwan University, Gyeonggi-do, Suwon, South Korea. ⁴These authors contributed equally: Hae Won Cho, Pavan Pujar. ✉email: yunseokkim@skku.edu; jclee@skku.edu; seonuk@skku.edu

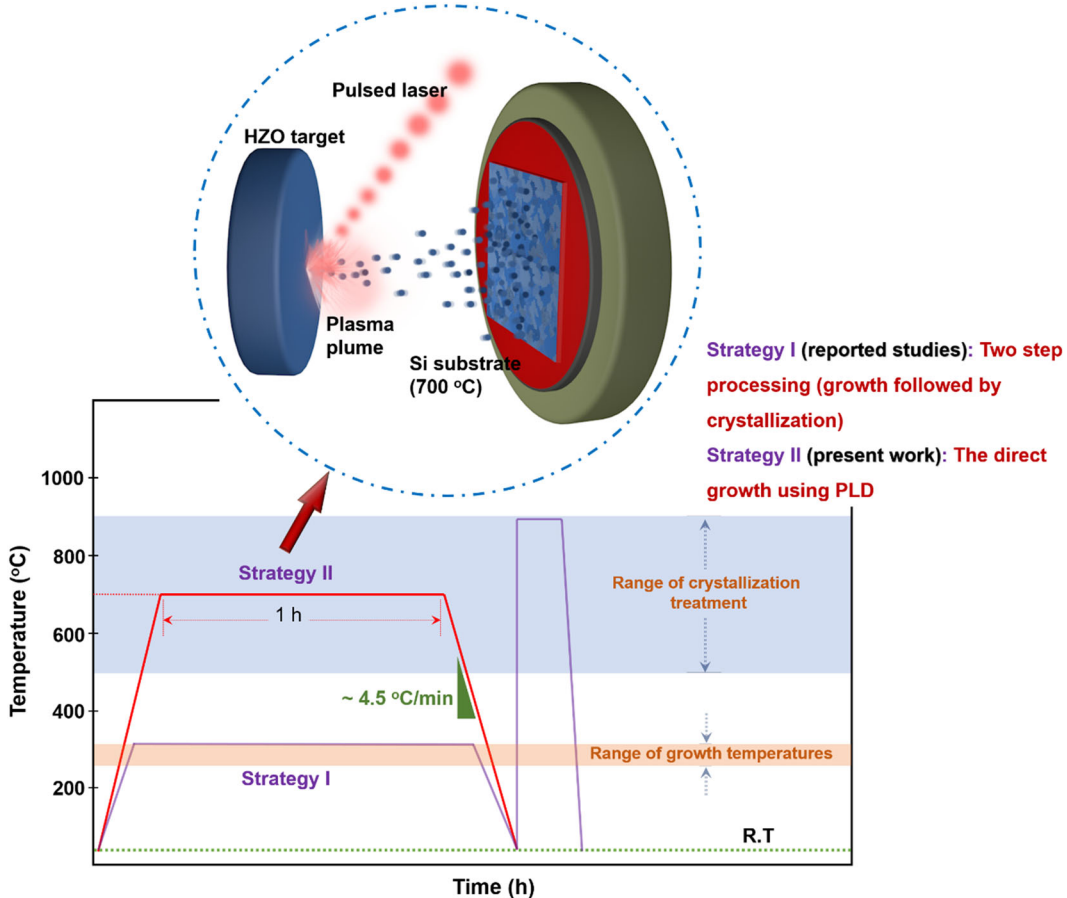


Fig. 1 Deposition and post-processing strategies using PLD and conventionally used ALD and CSD techniques. The schematic representing the growth of HZO thin film on preheated Si substrate (Note: R.T: Room temperature).

the various conceptual alternatives, in overcoming and/or nearing the thermionic limit, negative capacitance field-effect transistors (NCFETs) uses the amplification of channel surface potential more than the applied gate voltage. The negative capacitance (NC) effect transpires when the factor “ dP/dE ” is negative, where E is the electric field, and P is the ferroelectric polarization charge. This effect prevails under the switching of ferroelectric polarization^{14–16}. In this contribution, a multi-stacked gate insulator based on the ferroelectric-HZO grown using PLD and ALD grown HfO_2 afford MoS_2 NCFETs to be operated at a low input power and negligible-hysteresis¹⁷. The NCFETs operated below the thermionic limit dictated by Boltzmann’s Tyranny. The minimum SS obtained in both forward and reverse conditions are 33.03 ± 8.7 mV/dec and 36.42 ± 7.7 mV/dec, respectively.

RESULTS

Direct growth and characterization of $\text{Hf}_{0.5}\text{Zr}_{0.5}\text{O}_2$ on Si

Most previous studies (~85%) have focused on ALD-grown HZO, which is advantageous in achieving large-area and uniform thin films. However, it suffers not only from the difficulty of controlling process time but also utilization of toxic and costly volatile chemical precursors makes the technique capital intensive. Unlike ALD, PLD can control the growth rate and chemical composition of thin films through laser fluence, ambient gas pressure. Besides, by controlling the substrate temperature and cooling rate, thin films can be grown with high crystallinity¹⁸. PLD uses ceramic targets as a source of material to be deposited, allowing easy transfer of the target composition and making the process chemical-free and non-toxic. A schematic of the PLD technique for

the deposition of HZO thin films is presented in Fig. 1. Pulses of laser irradiation onto the HZO target allow the disintegration of the material from it and gets captured on to the pre-heated (700 °C) silicon substrate. In the case of ALD deposited thin films, the retained carbonaceous bonds are utilized to restrict grain growth during the post crystallization treatment³. This two-step process (growth followed by crystallization) has widely been reported and generalized to achieve metastable phases in HfO_2 based ferroelectrics (strategy I, Fig. 1). On the contrary, PLD grown HZO does not have growth retarders due to pure ceramic targets. Nevertheless, the sudden striking of HZO, which has disintegrated from the target surface, is subject to abrupt heating at the preheated silicon substrate. The HZO is allowed to crystallize on a silicon substrate, whose temperature is maintained to be 700 °C (strategy II, Fig. 1). Thus, in PLD grown HZO, an additional crystallization processing step stands inapplicable. In other words, the PLD technique amalgamates both thin film deposition as well as crystallization steps to grow crystalline HZO thin films. To understand the effect of working P_{O_2} the HZO thin films were grown at three different working P_{O_2} (= 0.1, 1, and 100 mTorr) with fixed cooling P_{O_2} (= 20 mTorr). Figure 2a depicts the X-ray diffraction patterns of HZO thin films grown.

The Bragg diffraction signatures at 28.3° and 34° correspond to m-phase and m-phase/tetragonal (t)-phase, respectively, while the diffraction peak centered at $\sim 30.2^\circ$ is attributed to polar o-phase. However, the slight shift in the Bragg angle from the reference, $\sim 30.5^\circ$, suggests that the HZO films are strained in the compressive in-plane state^{11–13}. Although the present thin films possess a mixed phase of m- and o- which is consistent with previous reports. Table 1 presents the status of present PLD grown

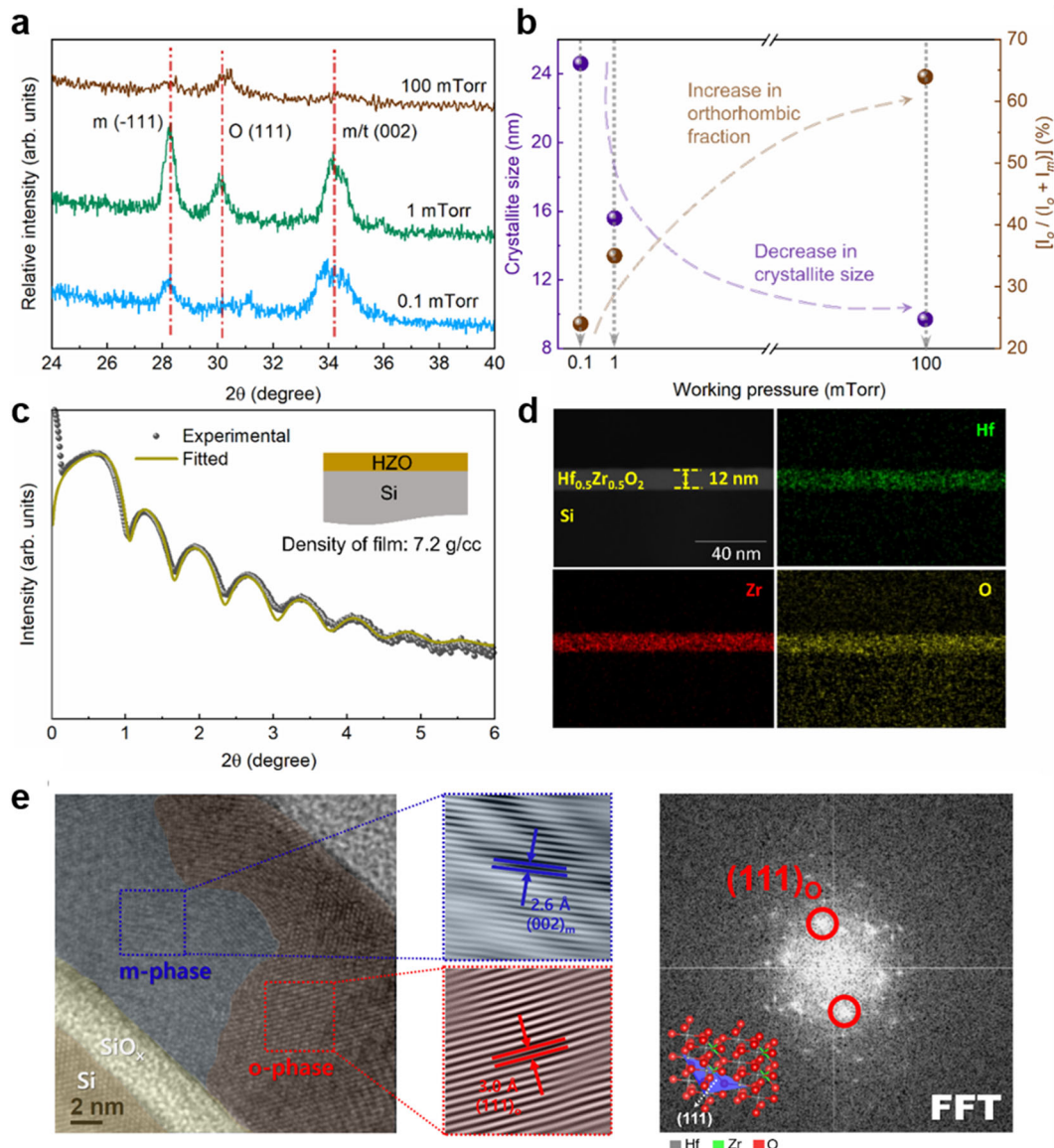


Fig. 2 Structural analysis of PLD-grown HZO on Si. a XRD diffractograms of HZO thin films deposited at different working P_{O_2} . **b** variation of crystallite size and the fraction of o-phase estimated from Scherrer equation and relative peak intensities. **c** XRR results for an as-deposited (working $P_{O_2} = 1$ mTorr) HZO thin film on Si. **d** TEM cross-sectional micrograph and EDS elemental mapping of HZO thin film; **e** Cross-sectional HR-TEM micrograph, filtered inverse FFT, and FFT pattern of the selected area.

HZO on Si substrate in comparison with previously reported studies. Most of the attempts are used to grow HZO via ALD, requiring an additional crystallization step. Furthermore, the crystallite size estimated from the Scherrer equation (Supplementary Table 1) for all working P_{O_2} conditions and it is found to decay with working P_{O_2} . Furthermore, the minimum of which is estimated to be ~ 9.7 nm. Consequently, the orthorhombic phase fraction estimated from the relative intensities of the diffraction responses (Eq. (1))¹⁹ is found to increase in thin films with an increase in the working P_{O_2} .

$$\text{Phase fraction} = \left[\frac{I_o}{(I_o + I_m)} \right] \times 100 \quad (1)$$

where, I_o and I_m are the relative intensities of diffraction responses of o- and m-phases, respectively. Although in the 0.1 mTorr and 100 mTorr cases, the intensities are not so prominent to estimate the relative fractions of the phases, the usual trend of diminishing m-phase concerning the 1 mTorr case is worth

H.W. Cho et al.

noting. Furthermore, these variations convey that the smaller grains contribute to large surface energy, being one of the requirements to stabilize the o-phase. The grain sizes possess a strong dependency on the thickness of the film. Thicker films generally promote grain growth due to the large volume of material in all directions. However, the thin films impose geometrical constraints to grain growth. The PLD grown HZO thin films (with constant thickness) have depicted minimum grain/crystallite sizes as a direct consequence of working P_{O_2} , which is of its first kind, ever reported in Fig. 2b. Apart from the smaller crystallites, it is essential to have pinhole-free thin films. The HZO thin film (working $P_{O_2} = 1$ mTorr) is presented as an example in Fig. 2c, where both the density and thickness of the film are estimated from X-ray reflectivity measurements, found to be 7.2 g/cc, 12 nm, respectively.

Furthermore, from a cross-sectional TEM micrograph, it is clear that the thin film possesses a thickness of ~ 12 nm (Fig. 2d). Thus, an ultrathin and dense film with finer grains is the ingredient for

Table 1. Comparison of previous reports of HZO thin films on Si substrate with the present study.

Deposition method	Post-deposition treatment	Characterization method	Phases			Reference
			m	o	t	
ALD	RTA	GIXRD	✓	✓	✗	1
ALD	RTA	--	✓	✓	✗	29
ALD	RTA	GIXRD	✓	✓	✗	36
ALD	RTA	GIXRD	✓	✓	✓	37
ALD	RTA	GIXRD	✓	✓	✓	38
ALD	RTA	--	--	--	--	39
PLD (Ar gas)	--	XRD	✓	✓	✓	22
PLD (O ₂ gas)	--	XRD	✓	✓	✓	Present work

RTA rapid thermal annealing, XRD X-ray diffraction, GIXRD grazing incidence X-ray diffraction, m monoclinic, o orthorhombic, t tetragonal.

the polar o-phase. In Fig. 2d, the TEM micrograph of the HZO thin film deposited at the same conditions depicts a uniform distribution of all individual elements throughout the film thickness. The cross-sectional HR-TEM micrograph reveals the polycrystalline nature of the HZO film (deposited with a working P_{O_2} of 1 mTorr). In Fig. 2e, The cross-sectional TEM micrographs and inverse FFT patterns reveal the planar d -spacing of two distinct phases (m-phase ~ 2.6 Å and o-phase ~ 3.0 Å)¹¹, which are in-line with the diffraction studies, depicting significant peaks of both the phases (Fig. 2a).

The surface chemical compositions of the PLD-HZO grown with three distinct working P_{O_2} = 0.1, 1, and 100 mTorr are analyzed using XPS, and the spectra are calibrated using carbon 1 s (C 1 s) peak positioned at 284.6 eV. The details of peak fitting and calibration using C 1 s are described in Supplementary Fig. 1 and Supplementary Tables 2–4. Furthermore, the presence of Hf and Zr at an expected ratio of 1:1 is confirmed, along with the oxygen from low- and high-resolution XPS spectra (Fig. 3a-b). Furthermore, the high-resolution O 1 s is deconvoluted into three synthetic signatures centered at 530.3 ± 0.1 eV, 531.7 ± 0.1 eV, and 532.6 ± 0.1 eV related to lattice oxygen (O^{2-}), oxygen vacancy (V_O) and surface adsorbed oxygen (O-ads) species, respectively (Fig. 3c)²⁰. From the ratio of relative area fractions of the principal components; it is confirmed that the ratio of oxygen vacancy to the lattice oxygen does not significantly depend on the selected range of working P_{O_2} (Supplementary Table 5). It is essential to understand the defect chemistry of ferroelectric-HZO, especially oxygen vacancies whose diffusion gives rise to leakage current in ferroelectric capacitors²¹.

Ferroelectric properties of the Hf_{0.5}Zr_{0.5}O₂

Furthermore, the HZO thin film deposited with a working P_{O_2} of 1 mTorr is probed to understand the ferroelectricity. Along with the previously analyzed 12 nm thick HZO, two more thin film samples with the thickness of 4 and 7 nm were deposited and whose film characteristics such as density and roughness were quantified through the x-ray reflectivity measurements (Supplementary Fig. 2). Figure 4a shows the polarization vs. voltage (P vs. V) response of HZO thin films, sandwiched between Si and TiN electrodes, within a voltage range of ± 5 V at a frequency of 10 kHz. The shape of the P-V curve conveys improved ferroelectric behavior compared to the previous report²². The reason behind the unsaturated P-V curve is attributable to the charge tunneling and lossy dielectric effect in the thin film^{23–25}. In Fig. 4b, the coercive voltage (V_c) and remnant polarization (P_r) values as a function of varying thickness (4, 7 and 12 nm) magnitudes are presented. The V_c and P_r tend to show an upward trend with the HZO thickness. Notably, the asymmetric ferroelectric response in

forward and reverse bias conditions are presented in Fig. 4b, which follows an inverse trend with the HZO thickness. The increasing thickness promotes a more symmetric P-V response. Thus, the higher thickness (i.e., 12 nm) depicts symmetric ferroelectric curve with large V_c and P_r magnitudes. The reason for such a behavior is believed to be relaxation of downward electric polarization due to the influence of the interfacial charge between HZO and Si^{26–32}. In addition, the current response of the Si/HZO/TiN devices for an input triangular voltage signal also depicts ferroelectric behavior (Supplementary Fig. 3). Furthermore, Piezo-response force microscopic (PFM) analysis is performed to obtain more insight into the ferroelectric phenomenon through understanding the surface polarization. To assess the local switching behavior of HZO thin film and confirm its switchability, box patterns with different signs of applied voltages and hysteresis loops are explored by PFM (Fig. 4d). As presented in Fig. 4e, upward and downward polarizations are switched in desired directions through applications of ± 5 V to the tip. This is evident from the phase difference ($\sim 180^\circ$) between two poled states (Fig. 4d). Furthermore, the PFM hysteresis loop (Fig. 4c) exhibits switchable behavior and seems similar to the P-V hysteresis loop observed in Fig. 4a. Given the strong ferroelectric response of 12 nm, thick HZO thin film is further adopted in the gate dielectric stack of NCFETs, to fetch the effect of negative capacitance with the high κ , amorphous HfO₂. The following section describes the performance of NCFETs with the MoS₂ channel.

Electronic properties of the MoS₂ NCFETs

Figure 5a shows the architecture of HZO-based MoS₂ NCFETs. In order to successfully utilize ferroelectricity of HZO in the devices, two essential factors are need to be considered. First, capacitance matching, which is fundamentally responsible in achieving stable NCFET operation. Since the metastable NC effect of ferroelectrics does not guarantee the stability of NCFET operation, a stable NC state can be achieved when a dielectric is connected in series with the ferroelectric layer and the stacked combination of those is used as a passive layer in place of a dielectric, in the regular device architecture. Matching the capacitance magnitudes results in the hysteresis-free operation of the devices, which is fundamentally distinct from the ferroelectric-FETs^{33,34}. The relation between capacitance and SS is expressed as: $SS = [1 + C_{semi}(C_{Fe}^{-1} + C_{ox}^{-1})] \times 60$ mV/dec. where C is the capacitance with subscripts, semi, Fe, and ox corresponds to semiconductor, ferroelectric and oxide dielectric, respectively³⁵. Given this, the capacitance of oxide dielectric must be greater than the ferroelectric to realize sub-60 mV/dec. switching. The phenomena is caused by the amplification of the surface potential (ψ_s) at the semiconductor-dielectric interface. As shown

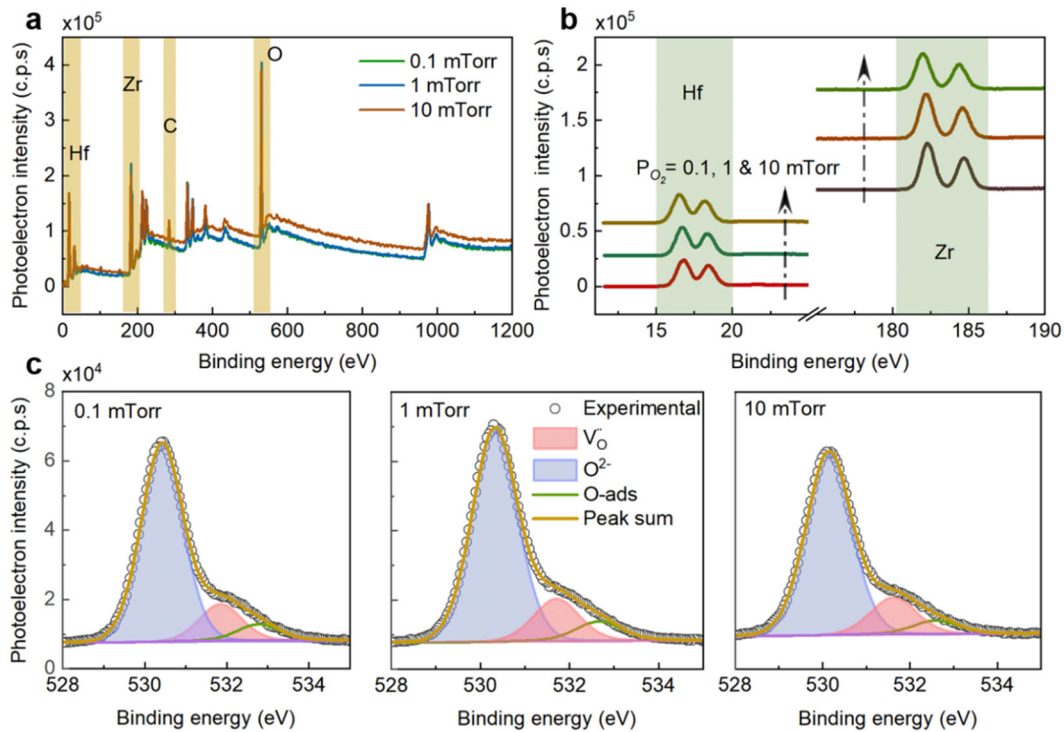


Fig. 3 Surface chemical composition of PLD-HZO thin films by XPS. a Survey spectra of HZO thin films grown with different working P_{O_2} (= 0.1, 1, and 100 mTorr). **b** high-resolution spectra of Hf 4f and Zr 3d for three cases of working P_{O_2} . **c** high-resolution O 1s spectra for three cases of working P_{O_2} .

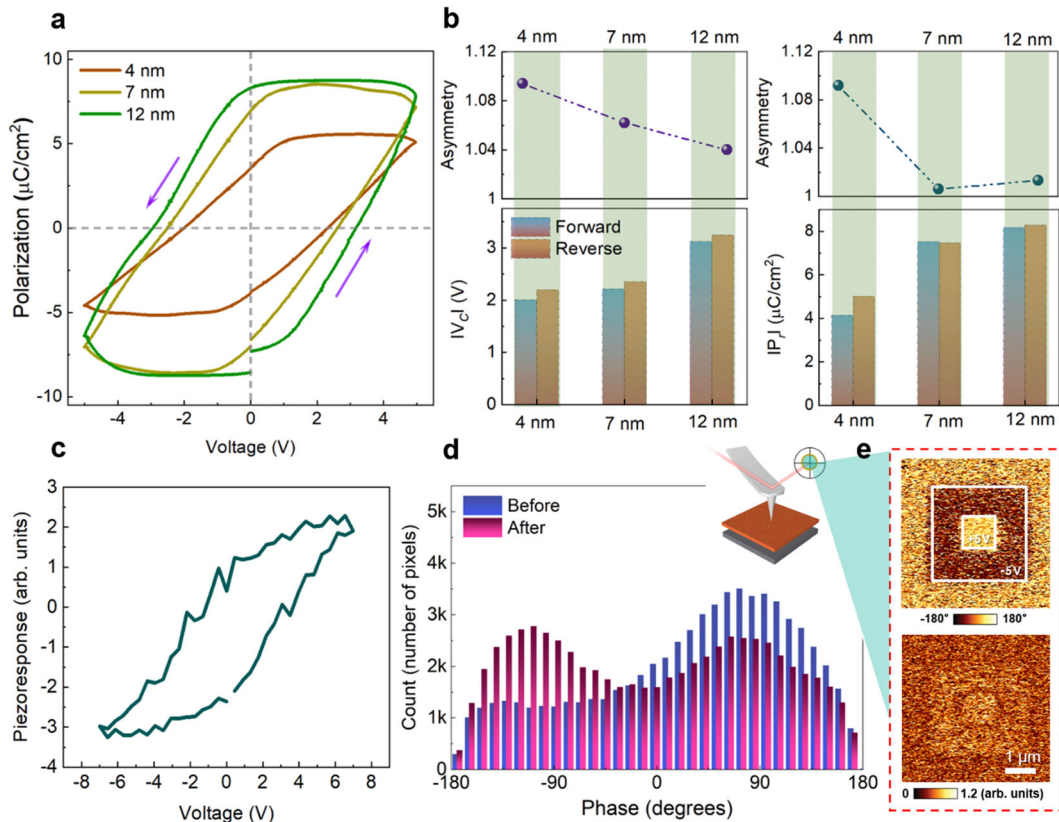


Fig. 4 Ferroelectricity of PLD-grown HZO on Si. Dependency of (a) P-V (at 10 kHz) curves (b) magnitudes of $|V_c|$, $|P_r|$ and curve-asymmetry on the thickness of HZO (4 nm, 7 nm, and 12 nm) (c) PFM hysteresis loop averaged from 25 measurements (d) Histograms of PFM phase, before and after poling, over the same area (e) PFM of HZO thin films after poling with applied tip voltages of ± 5 V.

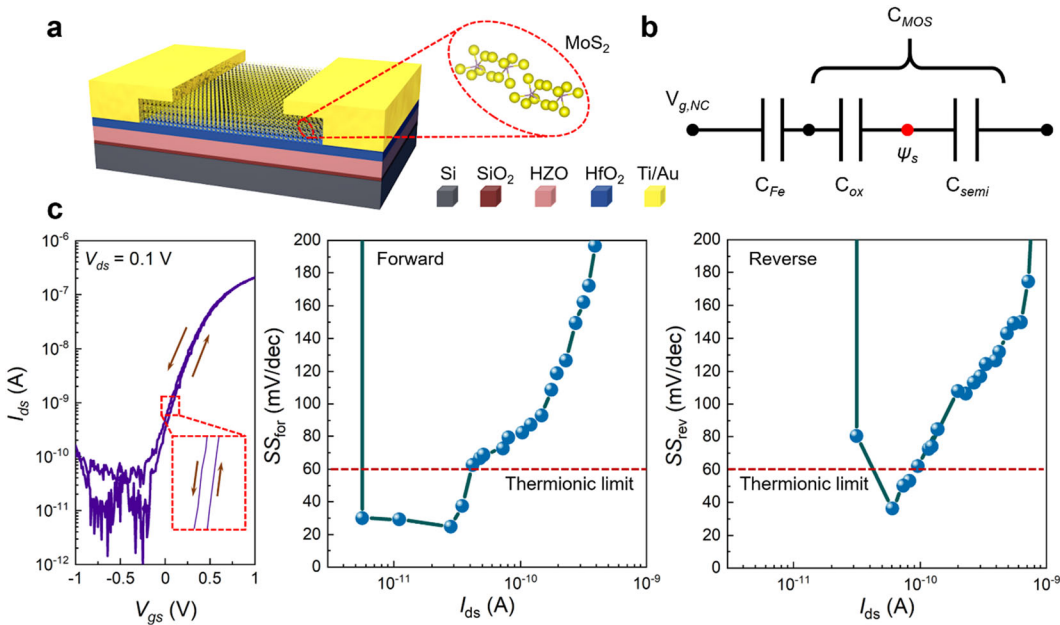


Fig. 5 Fabrication and electrical properties of MoS₂ NCFET. **a** Schematic of fabricated MoS₂ NCFET based on HZO with HfO₂ (9 nm). **b** Equivalent capacitance schematic of the MoS₂ 2D-NCFET ($V_{g,NC}$, ψ_s represents the negative capacitance gate voltage and surface potential, C_{MOS} , C_{semi} , C_{ox} , and C_{Fe} represent the capacitance of MOSFET, MoS₂, HfO₂, and HZO, respectively.) **c** Transfer characteristic curve (I_{ds} – V_{gs}) and SS versus I_{ds} characteristics of the MoS₂ NCFET at $V_{ds} = 0.1$ V.

in Fig. 5b, it is briefly expressed in the equivalent capacitance schematic of the MoS₂ NCFET. Second, the thickness of MoS₂; qualitatively thin film of MoS₂ is a suitable candidate semiconductor material for highly efficient gate modulation in low-power electronic devices³⁶. The optimized few layers of MoS₂ (~7 nm, Supplementary Fig. 4) is selected as the channel and transferred onto the HZO/HfO₂ surface via mechanical exfoliation. Use of thin MoS₂ is capable of minimizing the adverse charge trap effect leading to hysteretic behavior³⁵. The channel length of the fabricated devices is 15 μ m and the width is 28 μ m. Figure 5c shows I_{ds} – V_{gs} characteristics of MoS₂ NCFETs with a step size (ΔV_{gs}) of 0.01.

The maximum gate voltage range is maintained to be -1 to 1 V at a fixed V_{ds} ($=0.1$ V). From the transfer curve of the NCFET, a steep-switching behavior can be visualized, whose SS is considerably below the thermionic limit of 60 mV/dec, in both forward and reverse bias conditions. The SS_{for} and SS_{rev} of NCFETs are found to be 29.22 mV/dec. and 35.31 mV/dec., respectively, with negligible hysteresis of 28 mV (measured at a fixed I_{ds} of 1 nA). Statistically, the results measured on multiple devices is averaged to be 33.03 ± 8.7 mV/dec. and 36.4 ± 7.7 mV/dec., for SS_{for} and SS_{rev}, respectively. The significant reduction in SS magnitude is attributable to the NC effect offered by HZO thin films¹⁴. The amplification of voltage allowed the devices to work well within the physical limit set by Boltzmann's tyranny. Furthermore, the performance of the present NCFETs is compared with the previously reported data with various other ferroelectrics, such as CuInP₂S₆, P(VDF-TrFE), Al:HfO₂, and HZO (Supplementary Table 6)^{32–37}.

DISCUSSION

In this study, a ferroelectric HZO thin film is successfully grown at 700 °C on a silicon substrate using the PLD without any additional crystallization treatments. An optimum working P_{O_2} of 1 mTorr allows HZO to crystallize in the prominent ferroelectric- α -phase, which is confirmed by both XRD and HR-TEM analysis. The thin film with a maximum α -phase of 64% and a minimum crystallite size of ~9.7 nm has been achieved. Besides, the ~12 nm film

possesses uniform distribution of elements throughout the thickness. Furthermore, the evaluation of HZO ferroelectricity is comprehensively assessed by both P-V and PFM measurements. The PLD-grown HZO in the gate stack with HfO₂ is the key to overcome generic issues such as large hysteresis, threshold voltage instabilities, and large SS of MoS₂-based FETs. The introduction of the PLD grown ferroelectric HZO proved that the steep-switching device enables low-power operation at SS_{for} = 33.03 ± 8.7 mV/dec. and SS_{rev} = 36.4 ± 7.7 mV/dec. with free-hysteresis. Thus, the present work suggests a way to achieve low operating voltage of NCFETs coupled with smaller SS and negligible hysteresis. Also, the additional crystallization treatment may not always necessary to achieve ferroelectric α -phase in HZO. The present work is probably the report which demonstrates the feasibility of PLD grown ferroelectric HZO, without additional crystallization treatment, to be used to develop NCFETs, which can further be used in energy-efficient logic circuits.

METHODS

HZO growth on Si

PLD (KrF excimer laser, $\lambda = 248$ nm) deposition was used to grow HZO on a heavily doped $<100>$ p-type silicon (Si) wafer (resistivity $\leq 0.005 \Omega \cdot \text{cm}$). Initially, the Si substrate was cleaned by dipping it in buffered oxide etchant (6:1), which removes the native oxide layer. The cleaned Si substrate was then loaded into the PLD chamber in a high vacuum of 1.5×10^{-6} Torr. The substrate is allowed to reach 700 °C; meanwhile, laser fluence of 3 J/cm² along with the repetition rate of the laser pulse of 5 Hz was maintained. The deposition was carried out with a varied working oxygen partial pressure (P_{O_2}) of 0.1, 1, and 100 mTorr, while the oxygen pressure was kept 20 Torr during cooling.

Thin film characterization

The thin film structure was determined by X-ray diffraction (XRD: D8 DISCOVER) at the MEMS-Sensor Platform Center of SungKyunKwan University (SKKU). The high-resolution transmission electron microscopy (TEM: JEM-ARM 200 F, JEOL), coupled with energy-dispersive spectroscopy (EDS: Quantax-400, Bruker), was utilized at an accelerating voltage of 300 kV to estimate the thickness and elemental distribution. The chemical

composition was estimated by X-ray photoelectron spectroscopy (ESCA 2000 (MultiLab 2000)). The obtained XPS spectra were calibrated using the C 1 s peak positioned at 284.7 eV. Furthermore, the characteristics such as film density, roughness and thickness were estimated using X-ray reflectivity (XRR: Rigaku, smart lab). Planar TiN/HZO/Si capacitors were measured using a ferroelectric tester (Precision LC II, Radiant technologies). The PFM measurements were conducted using an atomic force microscope (AFM: Park Systems, NX-10) equipped with a lock-in amplifier (Stanford Research Systems, SR844), a function generator, and data acquisition systems (National Instruments, NI-PXle 5122/5412). PFM image measurements were performed with $0.7 V_{ac,rms}$ and 17 kHz. The PFM hysteresis loop was measured by applying a DC voltage ranging from -7 to $7 V_{dc}$ with a band excitation waveform of $1 V_{ac,peak}$ at 320–400 kHz. All AFM experiments were conducted using the conductive Pt/Cr-coated tip (BudgetSensors Multi75E-G).

Device fabrication and characterization

The PLD grown HZO layer on Si substrates were further subjected to the deposition (~ 9 nm) of high permittivity dielectric-HfO₂ at 250 °C using ALD (Lucida D100, NCD Co., Ltd., Daejeon, Korea). Multi-layered MoS₂ flakes (SPI Supplies, West Chester, PA, USA) were mechanically exfoliated using scotch tape and transferred on Si/HZO/HfO₂ stack. The AFM measurements were conducted for measuring MoS₂ thickness using an atomic force microscope (AFM: Park Systems, XE-7). Furthermore, E-beam-evaporated titanium/gold (20 nm/80 nm) was used as the top electrode. The source/drain was patterned by photolithography and the wet-etching process. The electrical properties of the fabricated devices were characterized using a semiconductor parameter analyzer (SCS-4200A, Keithley).

DATA AVAILABILITY

The data that support the findings of this study are available from the authors on reasonable request, see author contributions for specific data sets.

Received: 17 November 2020; Accepted: 1 April 2021;
Published online: 22 April 2021

1. Si, M. et al. Steep-slope hysteresis-free negative capacitance MoS₂ transistors. *Nat. Nanotechnol.* **13**, 24–28 (2018).
2. Zhirnov, V. V. & Cavin, R. K. Negative capacitance to the rescue? *Nat. Nanotechnol.* **3**, 77–78 (2008).
3. Chen, H. et al. Obvious ferroelectricity in undoped HfO₂ films by chemical solution deposition. *J. Mater. Chem. C* **8**, 2820–2826 (2020).
4. Mueller, S. et al. Incipient ferroelectricity in Al-doped HfO₂ thin films. *Adv. Funct. Mater.* **22**, 2412–2417 (2012).
5. Schroeder, U. et al. Lanthanum-doped hafnium oxide: a robust ferroelectric material. *Inorg. Chem.* **57**, 2752–2765 (2018).
6. Muller, J. et al. Ferroelectricity in simple binary ZrO₂ and HfO₂. *Nano Lett.* **12**, 4318–4323 (2012).
7. Kim, K. et al. Ferroelectricity in undoped-HfO₂ thin films induced by deposition temperature control during atomic layer deposition. *J. Mater. Chem. C* **4**, 6864–6872 (2016).
8. Triyoso, D. et al. Impact of film properties of atomic layer deposited HfO₂ resulting from annealing with a tin capping layer. *Appl. Phys. Lett.* **89**, 132903–132905 (2006).
9. Nikolau, N. et al. Influence of atomic layer deposition chemistry on high-k dielectrics for charge trapping memories. *Solid-State Electron.* **68**, 38–47 (2012).
10. Cho, D. Y. et al. Stabilization of tetragonal HfO₂ under low active oxygen source environment in atomic layer deposition. *Chem. Mater.* **24**, 3534–3543 (2012).
11. Wei, Y. et al. A rhombohedral ferroelectric phase in epitaxially strained Hf_{0.5}Zr_{0.5}O₂ thin films. *Nat. Mater.* **17**, 1095–1100 (2018).
12. Li, T. et al. Epitaxial ferroelectric Hf_{0.5}Zr_{0.5}O₂ thin film on a buffered YSZ substrate through interface reaction. *J. Mater. Chem. C* **6**, 9224–9231 (2018).
13. Lyu, J. et al. Growth window of ferroelectric epitaxial Hf_{0.5}Zr_{0.5}O₂ thin films. *ACS Appl. Electron. Mater.* **1**, 220–228 (2019).
14. Salahuddin, S. & Datta, S. Use of negative capacitance to provide voltage amplification for low power nanoscale devices. *Nano Lett.* **8**, 405–410 (2008).
15. Ko, E., Shin, J. & Shin, C. Steep switching devices for low power applications: negative differential capacitance/resistance field effect transistors. *Nano Convergence* **5**, 1–9 (2018).
16. Tu, L. et al. Field effect transistors: ferroelectric negative capacitance field effect transistor. *Adv. Electron. Mater.* **4**, 1870051 (2018).
17. Si, M., Lyu, X. & Ye, P. D. Ferroelectric polarization switching of hafnium zirconium oxide in a ferroelectric/dielectric stack. *ACS Appl. Electron. Mater.* **1**, 745–751 (2019).
18. Koster, G., Huijben, M. & Rijnders, G. *Epitaxial growth of complex metal oxides* (Elsevier, 2015).
19. Hsain, H. A., Lee, Y., Parsons, G. & Jones, J. L. Compositional dependence of crystallization temperatures and phase evolution in hafnia-zirconia (Hf_xZr_{1-x}O₂) thin films. *Appl. Phys. Lett.* **116**, 192901–192906 (2020).
20. Goh, Y., Cho, S. H., Park, S. H. & Jeon, S. H. Oxygen vacancy control as a strategy to achieve highly reliable hafnia ferroelectrics using oxide electrode. *Nanoscale* **16**, 9024–9031 (2020).
21. Pešić, M. et al. Physical mechanisms behind the field-cycling behavior of HfO₂-based ferroelectric capacitors. *Adv. Funct. Mater.* **26**, 4601–4612 (2020).
22. Nukala, P. et al. Direct epitaxial growth of polar (1-x)HfO₂-(x)ZrO₂ ultrathin films on. *Silicon Adv. Electron. Mater.* **1**, 2585–2593 (2019).
23. Florent, K. et al. Understanding ferroelectric Al:HfO₂ thin films with Si-based electrodes for 3D applications. *J. Appl. Phys.* **121**, 204103–204110 (2017).
24. Zhang, F. et al. Atomic layer deposition of Pb(Zr, Ti)O_x on 4H-SiC for metal-ferroelectric-insulator-semiconductor diodes. *J. Appl. Phys.* **109**, 124109–124112 (2011).
25. Vehkämäki, M. et al. Atomic layer deposition of ferroelectric bismuth titanate Bi₄Ti₃O₁₂ thin films. *Chem. Mater.* **18**, 3883–3888 (2006).
26. Zhu, Y. et al. Thickness-dependent asymmetric potential landscape and polarization relaxation in ferroelectric Hf_xZr_{1-x}O₂ thin films through interfacial bound charges. *Adv. Electron. Mater.* **5**, 1900554–1900560 (2019).
27. Wang, X. et al. Two-dimensional negative capacitance transistor with polyvinylidene fluoride-based ferroelectric polymer gating. *npj 2D Mater. Appl.* **1**, 1–7 (2017).
28. McGuire, F. A. et al. Sustained sub-60 mV/decade switching via the negative capacitance effect in MoS₂ transistors. *Nano Lett.* **17**, 4801–4806 (2017).
29. Xu, J. et al. Ferroelectric HfZrO_x-based MoS₂ negative capacitance transistor with ITO capping layers for steep-slope device application. *Appl. Phys. Lett.* **112**, 103104–103108 (2018).
30. Yu, Z. et al. Negative capacitance 2D MoS₂ transistors with sub-60mV/dec sub-threshold swing over 6 orders, 250 μ A/ μ m current density, and nearly-hysteresis-free. *IEEE International Electron Devices Meeting (IEDM)* 23.6.1–23.6.4. (2017).
31. Yu, Z. et al. Toward high-mobility and low-power 2D MoS₂ field-effect transistors. *2018 IEEE International Electron Devices Meeting (IEDM)* 22.4.1–22.4.4. (2018).
32. Wang, X. et al. Van der Waals negative capacitance transistors. *Nat. Commun.* **10**, 1–8 (2019).
33. Alam, M. A., Si, M. & Ye, P. D. A critical review of recent progress on negative capacitance field-effect transistors. *Appl. Phys. Lett.* **114**, 090401–090406 (2019).
34. Cao, W. & Banerjee, K. Is negative capacitance FET a steep-slope logic switch? *Nat. Commun.* **11**, 1–8 (2020).
35. Tu, L. et al. Ultrasensitive negative capacitance phototransistors. *Nat. Commun.* **11**, 1–8 (2020).
36. Nourbakhsh, A. et al. Subthreshold swing improvement in MoS₂ transistors by the negative-capacitance effect in a ferroelectric Al-doped-HfO₂/HfO₂ gate dielectric stack. *Nanoscale* **9**, 6122–6127 (2017).
37. Park, M. H. et al. Evolution of phases and ferroelectric properties of thin Hf_{0.5}Zr_{0.5}O₂ films according to the thickness and annealing temperature. *Appl. Phys. Lett.* **102**, 242905–242909 (2013).
38. Park, M. H. et al. The effects of crystallographic orientation and strain of thin Hf_{0.5}Zr_{0.5}O₂ film on its ferroelectricity. *Appl. Phys. Lett.* **104**, 072901–072905 (2014).
39. Si, M. et al. Steep-slope WSe₂ negative capacitance field-effect transistor. *Nano Lett.* **18**, 3682–3687 (2018).

ACKNOWLEDGEMENTS

This research was supported by the Basic Science Research Program of the National Research Foundation of Korea (NRF-2019R1A2C2002661, 2021R1A2B5B02002167, and 2021M3F3A2A03017873) funded by the Ministry of Science and ICT (2018R1A2B2003558).

AUTHOR CONTRIBUTIONS

H-W.C. and P-P. contributed equally to this work. M-S.C., S-H.K., S-I.H., J-W.P. and S-H.B. supported the experiment. Y-S.K., J-C.L. and S-K.K. managed and advised on this research.

COMPETING INTERESTS

The authors declare no competing interests.

ADDITIONAL INFORMATION

Supplementary information The online version contains supplementary material available at <https://doi.org/10.1038/s41699-021-00229-w>.

Correspondence and requests for materials should be addressed to Y.K., J.L. or S.K.

Reprints and permission information is available at <http://www.nature.com/reprints>

Publisher's note Springer Nature remains neutral with regard to jurisdictional claims in published maps and institutional affiliations.



Open Access This article is licensed under a Creative Commons Attribution 4.0 International License, which permits use, sharing, adaptation, distribution and reproduction in any medium or format, as long as you give appropriate credit to the original author(s) and the source, provide a link to the Creative Commons license, and indicate if changes were made. The images or other third party material in this article are included in the article's Creative Commons license, unless indicated otherwise in a credit line to the material. If material is not included in the article's Creative Commons license and your intended use is not permitted by statutory regulation or exceeds the permitted use, you will need to obtain permission directly from the copyright holder. To view a copy of this license, visit <http://creativecommons.org/licenses/by/4.0/>.

© The Author(s) 2021, corrected publication 2021